AGU PUBLICATIONS

Journal of Advances in Modeling Earth Systems

RESEARCH ARTICLE
10.1002/2013MS000286

Key Points:
- Implementation of a convection-based GW source parameterization into a GCM
- Explore physical aspects of convection-based GW source parameterization
- Physical GW parameterization improves QBO

Correspondence to:
S. Schirber,
sebastian.schirber@mpimet.mpg.de

Citation:
Schirber, S., E. Manzini, and M. J. Alexander (2014), A convection-based gravity wave parameterization in a general circulation model: Implementation and improvements on the QBO, *J. Adv. Model. Earth Syst.*, *6*, 264–279, doi:10.1002/2013MS000286.

Received 14 NOV 2013
Accepted 26 FEB 2014
Accepted article online 3 MAR 2014
Published online 25 MAR 2014

A convection-based gravity wave parameterization in a general circulation model: Implementation and improvements on the QBO

Sebastian Schirber[1], Elisa Manzini[1], and M. Joan Alexander[2]

[1]Max Planck Institute for Meteorology, Hamburg, Germany, [2]NorthWest Research Associates, Colorado Research Associates Division, Boulder, Colorado, USA

Abstract In order to simulate stratospheric phenomena, such as the Quasi-Biennial Oscillation (QBO), atmospheric general circulation models (GCM) require parameterizations of small-scale gravity waves (GW). In the tropics, the main source of GWs is convection, showing high spatial and temporal variability in occurrence and strength. In this study, we implement in the GCM ECHAM6 a source parameterization for GWs forced by convection. The GW source parameterization is based on the convective heating depth, convective heating rate, and the background wind. First, we show that the heating depth distribution of convective properties strongly influences the waves' source spectra. The strong sensitivity of spectral wave characteristics on heating property distributions highlights the importance of a realistic parameterization of convective processes in a GCM. Second, with the convection-based GW scheme as the unique source of GWs, the GCM simulates a QBO with realistic features. While the vertical extent of the easterly jet shows deficiencies, the wind speeds of the jet maxima and the variance of wind alteration show a clear improvement, compared to the standard model which employs a parameterization with constant, prescribed GW sources. Furthermore, the seasonality of the QBO jets downward progression is modeled more realistically due to the seasonality of physically based gravity wave sources.

1. Introduction

Tropospheric waves are the key elements in driving stratospheric dynamics, such as the prominent Quasi-Biennial Oscillation (QBO) of equatorial zonal winds. Due to the limited spatial resolution of atmospheric general circulation models (GCM), unresolved waves like gravity waves (GW) need to be parameterized. Focusing on the tropics, gravity waves are dominantly driven by convection, being highly variable in temporal occurrence and geographical distribution. However, parameterizations of gravity wave drag force include most commonly constant wave sources [*Scaife et al.*, 2000; *Giorgetta et al.*, 2002; *Shibata and Deushi*, 2005]. In this study, we implement a gravity wave source parameterization based on convection into the GCM ECHAM6, we show the dependence of the gravity wave momentum fluxes on the physical input properties, and we highlight improvements on the QBO amplitude and on the seasonality in the descent rate of QBO shear zones.

The QBO is a prominent dynamical phenomenon in the equatorial stratosphere [*Baldwin et al.*, 2001] characterized by a quasiperiodic oscillation of zonal winds with a period of ∼28 months. The QBO is driven by waves which emanate from the troposphere, propagate vertically into the middle and upper atmosphere, and deposit energy and momentum in the region of the waves' breaking levels. The horizontal scale of the waves spans several orders of magnitude, from planetary large-scale Kelvin and mixed Rossby-gravity waves over inertia-gravity waves down to small-scale gravity waves.

In the modeling world, the limited spatial resolution of GCMs requires a separation into resolved waves and parameterized gravity waves. Both wave components are essential in order to simulate stratospheric phenomena. Several GW parameterizations include two simplifying assumptions about GW source properties: (1) the source spectrum's shape of excited GWs is prescribed and (2) the source spectrum is constant in space and time. However, observations deviate from these assumptions: (1) GWs emanate from multiple sources which each show unique spectral characteristics depending on the source [*Alexander et al.*, 2010]. Besides orographically based GWs, whose effects are usually represented by a separate parameterization [*McFarlane*, 1987], GWs are generated by frontal systems, convection and more general tropospheric

instabilities. (2) These sources exhibit high spatial and temporal variability, implying similar variability for the excited GWs; for more details on GWs, see the review paper by *Fritts and Alexander* [2003]. Focusing on the tropics, theoretical [*Salby and Garcia*, 1987], observational [*Pfister et al*., 1993; *McLandress et al*., 2000; *Geller et al*., 2013], and numerical studies [*Alexander and Holton*, 1997; *Piani et al*., 2000; *Lane et al*., 2001; *Song et al*., 2003] attribute gravity wave activity in the stratosphere to the underlying convection. In the tropics, it is therefore reasonable to assume that convection plays the dominant role in GW generation.

Physically based source parameterizations take account of GWs excited by convection [*Chun and Baik*, 2002; *Beres et al*., 2004]. These parameterizations generate an interactive source spectrum based on the latent heating properties and the background wind. The advantages of such an approach concentrate on the following aspects. First, the amount of excited momentum flux shows a model-intrinsic temporal and spatial variability which, second, is also prone to changes on a climatological time scale. Third, the spectral shape depends on the physical properties of the modeled convective event, which removes the need to subjectively prescribe the shape of the source spectrum. The last aspect is emphasized by *McLandress and Scinocca* [2005] who show that three different GW propagation schemes can be tuned in a way to yield nearly identical responses on the drag profiles. The authors conclude that models would benefit rather from a more realistic source spectrum than from a better dissipation mechanism.

Several model studies implement aspects of a convection-based GW source parameterizations into GCMs. While *Geller et al*. [2011] add a prescribed seasonal variation in space and time on the amplitude of prescribed GWs, *Richter et al*. [2010] present a configuration of the Whole Atmosphere Community Climate Model (WACCM) with entirely physically based GW source parameterizations. *Lott and Guez* [2013] simulate a QBO with the GCM LMDZ, introducing a stochastic GW parameterization in which the waves' amplitudes are directly linked to the modeled heating rates. Concentrating on the QBO, *Kim et al*. [2013] show improvements of the simulated QBO in the Met Office Unified Model due to an implementation of the source parameterizations after *Chun and Baik* [2002], which generates roughly 50% of the total GW fluxes in the tropics.

In this study, we analyze effects of a convection-based gravity wave scheme which represents the unique source of tropical GWs in an atmospheric GCM. Given this configuration, we are able to show the full effect of the source variability on the mean stratospheric state. We further highlight the sensitivity of the GW source parameterization to the convection scheme and isolate the properties which dominate the different spectral characteristics of the source spectra.

2. Experimental Setup

2.1. A Climate Model With Three GW Parameterizations

We use the atmospheric general circulation model ECHAM6 [*Stevens et al*., 2013], the latest version of the atmospheric component of the earth system model developed at the Max Planck Institute for Meteorology (MPI-ESM) [*Giorgetta et al*., 2013]. The simulations performed here use a spectral truncation at wave number 63 and an associated Gaussian grid of $\sim 1.9^\circ$ resolution. The vertical grid consists of 95 hybrid sigma pressure levels, with a spacing of roughly 700 m in the lower stratosphere, resolving the atmosphere from the surface up to 0.01 hPa. In ECHAM6, the parameterization of cumulus convection is based on the mass-flux scheme by *Tiedtke* [1989] with modification for deep convection incorporated by *Nordeng* [1994]. The model parameterizes the effects of unresolved, nonorographic GWs with a scheme after Hines which is based on the Doppler spread theory [*Hines*, 1997a, 1997b]. The prescribed spectrum of waves emanating from the troposphere is broad band with constant amplitude in time and space, although in the standard model setup, a latitudinal amplitude enhancement is introduced around the equator in order to obtain a QBO with a realistic period [*Schmidt et al*., 2013].

In addition to the Hines scheme, we implement the convection-based GW source parameterization after *Beres et al*. [2004] which is coupled to the GW propagation parameterization after *Alexander and Dunkerton* [1999]. Since convection is the primary source of tropical GW, which are covered by the Beres scheme, we disable the Hines scheme within the tropics (latitude $|\Phi| \leqq 20^\circ$) entirely by setting u_{rms}, the parameter for the source strength, to 0 m/s. Outside the tropics, the Hines scheme increases linearly between $20^\circ \leqq \Phi \leqq 30^\circ$ and remains constant with u_{rms} at 1 m/s in the extratropics ($|\Phi| \geqq 30^\circ$). This somewhat arbitrary latitudinal partition of the two GW parameterizations is based on the latitudinal extent of the Beres scheme, shown

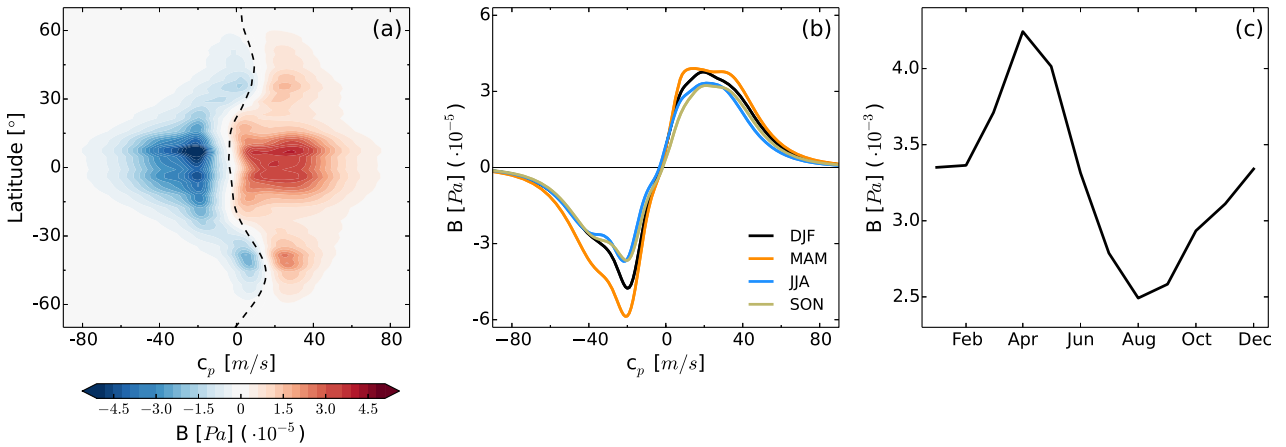

Figure 1. Source spectrum *B* of zonal momentum flux and its seasonal variability. (a) Latitudinal distribution of time and zonal mean source momentum flux as a function of phase speed. The dashed black line shows the zonal mean wind at 700 hPa, the basis for the Doppler shift of the spectrum. (b) Zonal and meridional (5°N to 5°S lat) mean source spectra of zonal momentum flux in the four seasons. (c) Annual cycle of total zonal momentum flux *B*, zonal and meridional (5°N to 5°S lat) mean integrated over phase speed. All time averages cover 30 years (Figures 1a–1c).

in Figure 1 which is discussed in more detail in section 3. The orographic GW scheme [*Lott and Miller*, 1997] is primarily active in the extratropics and remains untouched in this model setup. In the chosen setting with the nonorographic Hines and Beres GW source parameterizations, the Beres scheme produces additional wave momentum flux in the extratropical regions of the storm tracks. We decide to include this contribution for two reasons: first the additional drag does not deteriorate the model's zonal mean circulation (not shown); second, an arbitrary and artificial latitudinal restriction to the tropics is not based on physical arguments.

2.2. Mechanisms of a Convection-Based GW Scheme and Implementation

The Beres scheme produces a spectrum of gravity waves depending on the latent heating properties and the background wind in grid boxes with active convection. The parameterization generates an individual distribution of wave momentum flux $B_0 = \overline{u'w'}$ in $[m^2/s^2]$ as a function of horizontal phase speed c_p in (m/s). The shape and amplitude of the individual source spectra are dependent on the heating depth, the heating rate, the mean wind in the heating region, and several prescribed parameters, each described briefly in the following paragraphs. For a more quantitative description including a theoretical derivation and detailed equations for the spectrum of source momentum flux see *Beres et al*. [2004].

The vertical extent of condensational heating within a cloud, the heating depth H_q, governs the dominant vertical wavelength of the excited waves. Since the vertical wavelength translates to a horizontal phase speed, the heating depth determines the position of the maxima in the phase speed spectrum. Large heating depths generate GW spectra peaking at high phase speeds, whereas small heating depths generate GW spectra peaking at low phase speeds. Being an equally important input variable, the vertical mean heating rate Q_0 strongly influences the overall amount of momentum flux, the wave's amplitude. In the employed GCM, the convection parameterization does not provide information about individual convective events and the associated heating properties, like Q_0, of these subgrid scale events. The bulk mass flux scheme rather gives mean heating properties of all single convective events occurring within one grid box. Under the assumption that the mean effect of all individual convective events is realistically represented by the bulk scheme, we estimate the heating rate in a simple approach as

$$Q_0 = \frac{Q_{max}}{C_F} \tag{1}$$

with Q_{max} being the peak heating rate within the GCM grid box and C_F the fraction of convection, which is assumed to be a constant 3.5% of a grid box. We highlight that the heating rate acts strongly nonlinear on the wave amplitudes: $B_0 \propto Q_0^2$, see equation (30) in *Beres et al*. [2004]. Therefore, the heating rate

characteristics of the convection scheme, and in particular heating rate distributions at different heating depths, are crucial for the shape of the GW source spectrum.

The horizontal wind shear across the vertical extent of the heating governs the asymmetries of the source spectra. The wind shear $\langle\frac{\partial U}{\partial z}\rangle$ is calculated as the mean background wind relative to the wind at 700 hPa height via

$$\left\langle \frac{\partial U}{\partial z} \right\rangle = \int_{H_b}^{H_t} (u(h) - u_{700}) \mathrm{d}h \tag{2}$$

with H_b the cloud base and H_t the cloud top, $u(h)$ the horizontal wind speed projected onto the plane of the horizontal wind at 700 hPa, u_{700}, which is assumed to act as the steering level of the convective cell. Given a positive wind shear $\langle\frac{\partial U}{\partial z}\rangle$, momentum fluxes with negative phase speeds relative to u_{700} dominate the spectrum and vice versa [*Pfister et al*., 1993]. The reason for this upstream enhancement of momentum fluxes is twofold. On one hand, a mechanism similar to critical level filtering reduces momentum fluxes of waves propagating in the direction of the storm-relative mean wind. On the other hand, a mechanism similar to the "obstacle effect" increases momentum fluxes of waves propagating in the opposite direction of the storm-relative mean wind; see *Beres et al*. [2002] for a more detailed explanation. The horizontal orientation of phase speeds is determined by the steering level of a convective cell, chosen as the horizontal wind at 700 hPa. Analogous to the assumption in the previous paragraph about mean grid box heating, we assume that the mean grid box values of wind are representative for wind of the convective fraction of the grid box. In the two azimuths of wave orientation, the phase speeds are Doppler shifted with respect to the wind speed at 700 hPa. The source spectrum spans waves from -100 m/s to 100 m/s with a resolution of 1 m/s.

In contrast to the preceding input variables, which are interactively given by the GCM at each time step, the source parameterization also requires several constant parameters which need to be prescribed. Following the nomenclature from *Beres et al*. [2004], we use $L = 1000$ km for the spatial averaging domain and $\sigma_x = 3.5$ km for the horizontal extent of the individual convective cell. The parameterization initiates waves only when the convection scheme is active and omits shallow convection by applying a minimum heating depth of 2.5 km. In order to account for the earth's sphericity, the source spectrum is scaled by latitude with $B = \rho_0 \cdot B_0 \cdot \cos(\Phi)$. Waves are launched at the cloud top, with ρ_0 in B the density at cloud top, from where the propagation routine by *Alexander and Dunkerton* [1999, hereafter AD99] calculates for each individual phase speed bin its corresponding breaking level in the atmosphere above. The scheme with modifications after *Ortland and Alexander* [2006] is based on the simple assumption that momentum fluxes carried by waves are deposited entirely at the initial onset of linear instability. Given the background wind and density profiles, this concept allows a mapping of a tropospheric spectrum of momentum flux to mean flow acceleration in the layers above. We use a horizontal wavelength $\lambda_h = 1000$ km and an intermittency factor $\epsilon = 0.003$. For a detailed explanation of the concept of intermittency, see *Alexander and Dunkerton* [1999]. In our application with 201 discretely resolved spectral phase speed bins, $\epsilon \cdot 201 \simeq 0.6$ describes the occurrence of any spectral point, a value of order one.

2.3. Experiments and Observational Data Sets

We explore the effects of the Beres scheme, coupled to AD99 (ECHAM6-Beres), in comparison with a control run, which includes a GW parameterization with constant GW sources (ECHAM6-Hines). For both experimental setups, we perform a 30 year atmospheric simulation with prescribed climatological sea-surface temperatures (SST) and sea-ice concentrations (SIC), compiled from observed SSTs and SICs. We use monthly mean values of 30years as standard temporal resolution for the shown plots, but model data to compile Figures 2, 4, and 5 consist of 6 hourly instantaneous output covering 5 years. In order to evaluate zonal winds U of the two model setups, we use two different reanalysis products, NCEP [*Kistler et al*., 2001] and ERA-Interim [*Dee et al*., 2011]. For the EOF analysis of section 4.2.2, we use monthly mean zonal winds based on radiosonde observations at three equatorial stations and compiled at Freie Universität Berlin (FUB) (http://www.geo.fu-berlin.de/en/met/ag/strat/produkte/qbo/).

For the evaluation of quantities of the convection scheme in section 3.3, we derive from observations two quantities: a maximum heating rate distribution and a cloud top distribution. First, the heating rates are

derived from rain rates provided by Tropical Rainfall Measurement Mission (TRMM) using the algorithm [*Ryu et al*., 2011] that includes both convective and stratiform rain types. Second, cloud top heights are derived from global merged infrared satellite measurements of brightness temperature using the NCEP reanalysis to estimate height [*Ortland et al*., 2011]. Note that the two employed observational quantities are not measured directly but are rather products derived from observations. Therefore, retrieval errors in the original observations and simplified assumptions in the derivation of the final product introduce additional uncertainty. In order to compare cloud observations with model data in a consistent way, we use temporally instantaneous data every 3 h covering the year 2007 and we remove noncloudy data points and average observations spatially on $2^\circ \times 2^\circ$ resolution before performing the analysis.

3. A Variable Source Spectrum of GW Momentum Flux

In this section, we highlight the fundamental aspects that are introduced by a convection-based parameterization for gravity waves. First, we examine the temporal and spatial distribution of excited momentum flux, concentrating on the overall amount of momentum flux by integrating the source spectrum. In the second step, we look in more detail at the spectral characteristics of the source spectrum and provide the link between resolved input quantities, such as background wind and convective properties, and source spectrum properties, like its shape and its asymmetry. Having identified the decisive properties of the input quantities, we evaluate the quantities produced by the model with observational data sets.

As described in section 2.2, waves are launched along the direction of u_{700} which results in a meridional and zonal component in wave forcing and drag. Since the orientation of u_{700} is oriented dominantly in the zonal direction, the source spectrum in the meridional direction only reaches approximately 30% of the wave amplitude in zonal direction (not shown). Because we additionally focus on the zonally oriented winds of the QBO, we restrict the following analysis to zonal components even though waves are also launched in the meridional direction.

3.1. Spatial Distribution and Seasonality of Momentum Flux

The GW source spectrum of momentum fluxes from the Beres scheme shows temporal and spatial variability due to the parameterization's coupling to resolved quantities. Largest source momentum fluxes occur in tropical regions, $|\Phi| < 20^\circ$, where convection is most active throughout the year, see Figure 1a. However, the parameterization also initiates waves in the midlatitudinal regions of the storm tracks, which are more active in the southern hemisphere. Since cloud heating depths are bigger in the tropics than in the midlatitudes, the wave spectrum peaks at and extends to higher phase speeds in the tropics compared to the midlatitudes. The phase speed spectrum is Doppler shifted with respect to the 700 hPa zonal wind which is particularly important at the midlatitudes where a nonzero background wind prevails. In the tropics, however, mean background winds are small which leads to a source spectrum with peak momentum fluxes at about $+20$ m/s and -20 m/s phase speed; see Figure 1b. The source spectrum compares well in latitudinal distribution with results from the WACCM model with the same GW source parameterization [*Beres et al*., 2005; *Richter et al*., 2010]. Besides differences in the convection parameterization between the two model versions, the implementation of the Beres scheme in WACCM also includes a base limit for when the Doppler shift is applied: Only when the wind speed at 700 hPa is above 10 m/s, the phase speeds of the source spectrum are Doppler shifted. An inclusion of this base limit into our code would generate a source spectrum with momentum fluxes dominating at positive phase speeds (not shown). However, we remove this somewhat arbitrary, limit on the Doppler shift in our implementation of the code. Therefore, while positive phase speeds dominate the source spectrum in the WACCM model, ECHAM6-Beres shows more momentum flux at negative phase speeds than at positive phase speeds.

The source momentum flux shows a strong seasonal cycle, manifested in the mean seasonal spectra and the annual cycle of integrated source momentum flux shown in Figures 1b and 1c. The amount of momentum flux peaks in spring and shows a minimum in late summer, which quantitatively represents a reduction of approximately 40% from the peak in April to the minimum in August. The seasonality in source momentum flux is the basis for further analysis on the seasonality of the QBO in section 4.2.

It would be desirable to be able to identify a single physical input quantity which causes the seasonality in the amount of excited momentum flux B of Figure 1c. Even though the seasonality of the heating rate Q_0 is

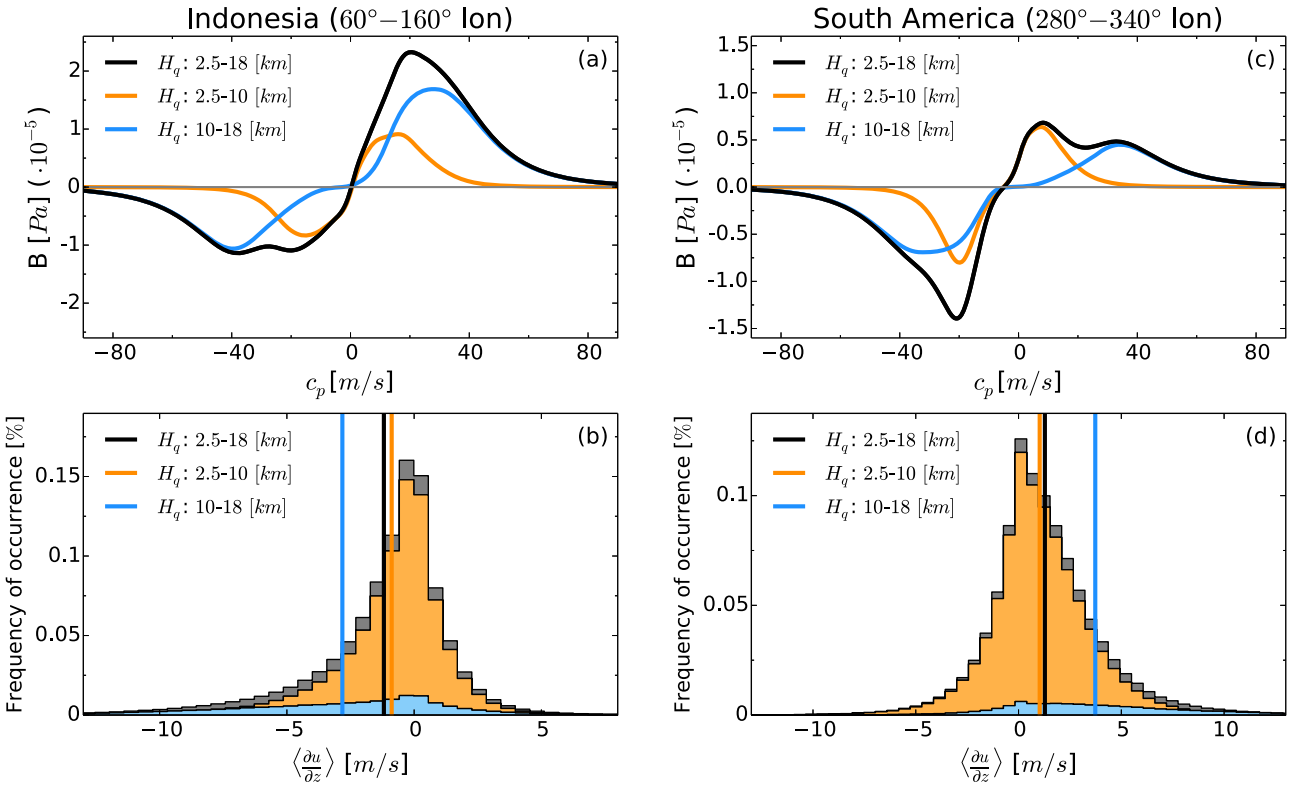

Figure 2. Effect of the background wind on the source spectrum, shown for two selected regions, centered over (a and b) Indonesia (60°–160° lon) and over (c and d) South America (280°–340° lon). Colors illustrate different regimes of heating depth: contribution from shallow heating depths (2.5–10 km, orange) and from large heating depths (10–18 km, blue) to the entire range (2.5–18 km, black). Zonal, meridional (5°N to 5°S lat), and time (5 years) mean source spectra of zonal momentum flux (Figures 2a and 2c). The spectral asymmetry is caused by wind shear $\langle \frac{\partial U}{\partial z} \rangle$, relative to the zonal wind at 700 hPa, within the vertical extent of the heating. The histogram of wind shear $\langle \frac{\partial U}{\partial z} \rangle$ is shown for different regimes of cloud heating depths (Figures 2b and 2d) while the vertical lines denote the distribution mean.

dominating the seasonality of *B* (not shown), we cannot isolate a single, unique physical quantity which fully explains the seasonal cycle of *B*. Besides the seasonality in Q_0, variability in tropospheric wind shear and other convective properties also contribute to the seasonal cycle in the amount of source momentum flux. In the following two sections, however, we individually highlight the two most relevant physical input quantities, the background wind and the convective heating properties, which decisively control the characteristics of the source spectrum.

3.2. Effect of the Background Wind on the Source Spectrum

We show the effect of the background wind on the source spectrum for two selected regions, centered over the Indonesian archipelago and over South America. The source spectra in these two regions exhibit strong asymmetries, favoring momentum fluxes with positive phase speeds over Indonesia and momentum fluxes with negative phase speeds over South America; see Figures 2a and 2c. The asymmetries are dominated by deep convective clouds, depicted by the blue curve, whereas the contribution of the more shallow clouds is almost symmetric, depicted by the orange curve in Figures 2a and 2c.

As outlined in section 2, a positive wind shear produces a source spectrum with dominating negative phase speeds and vice versa. This result from a case study with a cloud resolving model [*Beres et al.*, 2002] and localized observations [*Pfister et al.*, 1993] is now extended to large geographical regions by model data of GWs generated with linear theory [*Beres et al.*, 2004]. The histogram of wind shear $\langle \frac{\partial U}{\partial z} \rangle$ in Figures 2b and 2d shows a clear nonzero mean value, especially for the regime of deep convective clouds which cause the spectral asymmetry. While a negative wind shear leads to a source spectrum with dominant positive phase speeds over Indonesia, a positive wind shear can be associated with a source spectrum with dominant negative phase speeds over South America.

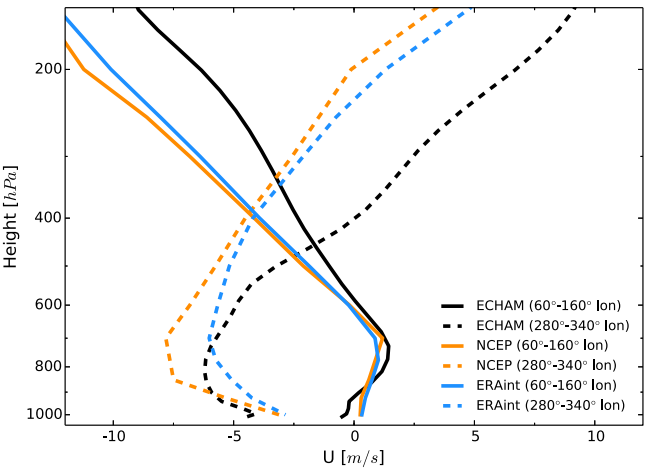

Figure 3. Zonal, meridional (5°N to 5°S lat), and time mean vertical wind profile for two regions, covering the eastern Indian Ocean and Indonesia (60°–160° lon, solid) and South America (280°–340° lon, dashed). Comparison of ECHAM6-Beres simulation (black) with two reanalysis products: NCEP (orange) and ERA-Interim (blue). ECHAM6-Beres covers 30 years, NCEP 62 years, and ERA-Interim 20 years.

The modeled wind shear over the two selected regions agrees with reanalysis data, see Figure 3. While ECHAM shows a westerly bias in the upper troposphere in both regions, the vertical wind shear in the model is qualitatively consistent with reanalysis. In the free atmosphere, the region centered over the Indonesian archipelago shows a negative wind shear and the region over South America a positive wind shear. To summarize this subsection, different background winds, which qualitatively agree with reanalysis products, cause significant asymmetries in the GW source spectrum in large geographical regions.

3.3. Effect of Convective Heating Properties on the Source Spectrum

The source momentum fluxes show a strong dependence on properties of the convection scheme. The most important quantities are the heating depth and the maximum heating rate within a GCM grid box, with a particular importance on the histogram of heating depth and the heating rate's dependence on heating depth. The emitted source momentum flux is separated into the two regimes of shallow (orange) and deep (blue) convective clouds, see Figure 4, illustrated by the peak at higher phase speeds for deep convective clouds. The total spectrum (black) results from a superposition of both heating depth regimes. The separation into two heating depth regimes can be observed in more detail in Figure 5a, which shows the amount of excited momentum flux B as a function of heating depth. Shallow clouds with 2.5 and 5 km heating depth and deep convective clouds with around 15 km heating depth contribute significantly to the entire source spectrum. Convective clouds with heating depths in the range 6–12 km, however, produce very little momentum flux.

The momentum flux histogram in Figure 5a corresponds only partly to the heating depth histogram in Figure 5b, which shows that the convection scheme produces most frequently rather shallow clouds (<6 km), very few midlevel clouds (6–12 km) and some deep convective clouds (>12 km). The two histograms do not agree because the amplitude of the source spectrum is additionally scaled by a factor $\propto Q_{max}^2$ which strongly increases with increasing heating depth, see Figure 5c. This nonlinear amplification of the source spectra's amplitudes leads to a peak in B at large heating depth, even though convection with large heating depth does not occur very frequently.

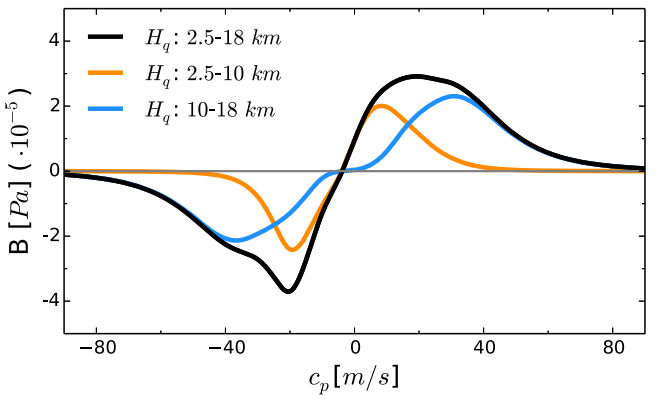

Figure 4. Separation of source spectrum into regimes of heating depth H_q. Zonal, meridional (5°N to 5°S lat), and time (5 years) mean source spectrum B for all cloud heating depths (black), shallow cloud heating depths (orange), and deep cloud heating depths (blue).

A comparison with TRMM and satellite-based observations reveals deficiencies in the convection scheme, most apparent in the histogram of heating depth, see Figure 5b. Observations show a continuous distribution with dominating midlevel convection which peaks at 9 km and ends at 12 km heating depth rather than the double peak distribution that the convection scheme produces. Most obvious discrepancy appears in the range of 6–12 km

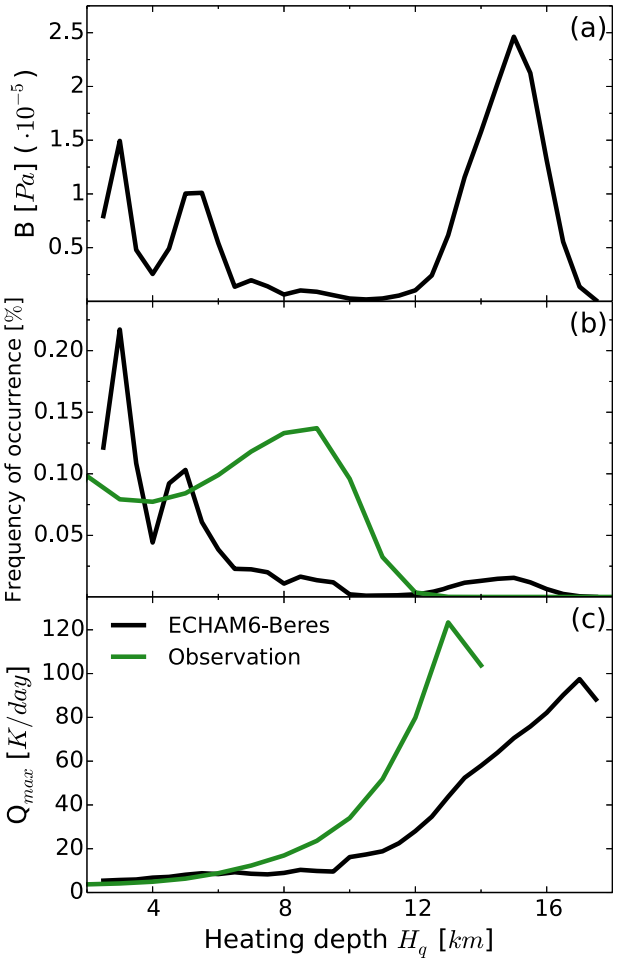

Figure 5. Influence of convection properties on the (a) source momentum flux *B* as a function of heating depth. (b) Heating depth distribution and (c) maximum heating rate within a GCM grid box (black) are compared to estimated observations (green) derived from geostationary infrared satellite data and TRMM.

heating depth, where the model lacks convection, and at large heating depths, where the model produces convection in contrast to the observations. For a more detailed discussion and consequences due to the difference in observations and model data, see section 5. The model's distribution of heating rate Q_{max}, however, compares qualitatively to the observations, see Figure 5c, with a strong increase in Q_{max} with increasing heating depth. The kinks at the upper end of the distributions should not be overinterpreted since these are prone to sampling errors due to the very small number of events at the upper end of the heating depth distribution.

4. The QBO

ECHAM6-Beres produces a QBO with realistic features, see Figure 6. The simulated evolution of zonal winds shows prominent features of the QBO: a periodic alternation of westerly and easterly winds, an asymmetry in amplitude with easterly jets being stronger than westerly jets, and a mean period of ∼27.5 months. The simulated period is tuned with the parameters C_F and L, see section 2 for a more detailed parameter description and section 5 for a more thorough discussion on parameter tuning.

4.1. Comparison With ECHAM6-Hines and ERA-Interim

A comparison with the QBO of ECHAM6-Hines and of ERA-Interim shows improvements and deficiencies of the QBO simulated with ECHAM6-Beres. Both ECHAM6-Hines and ECHAM6-Beres produce a QBO with too strong westerly jet maxima, Figure 7. However, this bias is strongly reduced in ECHAM6-Beres. Also, the bias in the easterly jet maxima of ECHAM6-Hines is reduced such that the wind speed maximum in ECHAM6-Beres agrees with reanalysis. The easterly jet in ECHAM6-Beres does not extend as far downward as in reanalysis data, but ends at 50 hPa rather than 90 hPa as in the reanalysis, which could partly be a result of the generally weaker easterly jet in ECHAM6-Beres. The westerly jet extends toward ∼75 hPa in both model simulations and agrees well with ERA-Interim. In both model simulations, the QBO extends too far into the upper stratosphere above 10 hPa, with an improvement in ECHAM6-Beres. However, this improvement comes at the cost of pronounced easterlies at about 1 hPa in ECHAM6-Beres.

The zonal wind variances in ECHAM6-Beres agree well with reanalysis, see Figure 8. The wind variance in QBO-related periods agrees not only in amplitude but also in the position of the peak, a clear improvement over ECHAM6-Hines. The wind variance at 1 hPa in ECHAM6-Beres agrees reasonably well with ERA-Interim. At higher altitudes around 0.1 hPa, ECHAM6-Beres simulates the decrease in wind variance more realistically than ECHAM6-Hines, but shows higher values than the reanalysis.

The improvement in QBO wind variance in ECHAM6-Beres can partly be explained by different drag profiles in ECHAM6-Beres and ECHAM6-Hines. Figure 9 compares drag profiles from simulations performed over

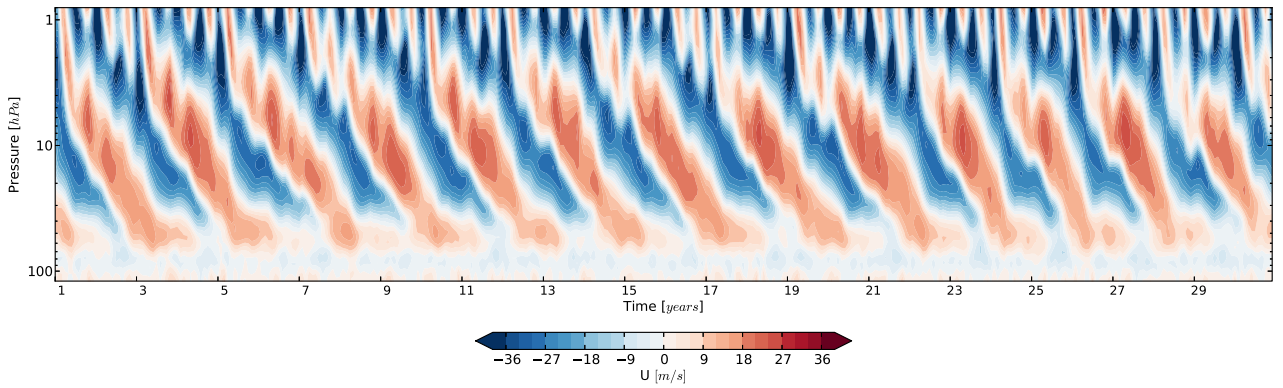

Figure 6. The QBO. Time series of meridional (5°N to 5°S lat) and zonal mean zonal wind from a 30 year model run with a purely convection-based gravity wave source parameterization.

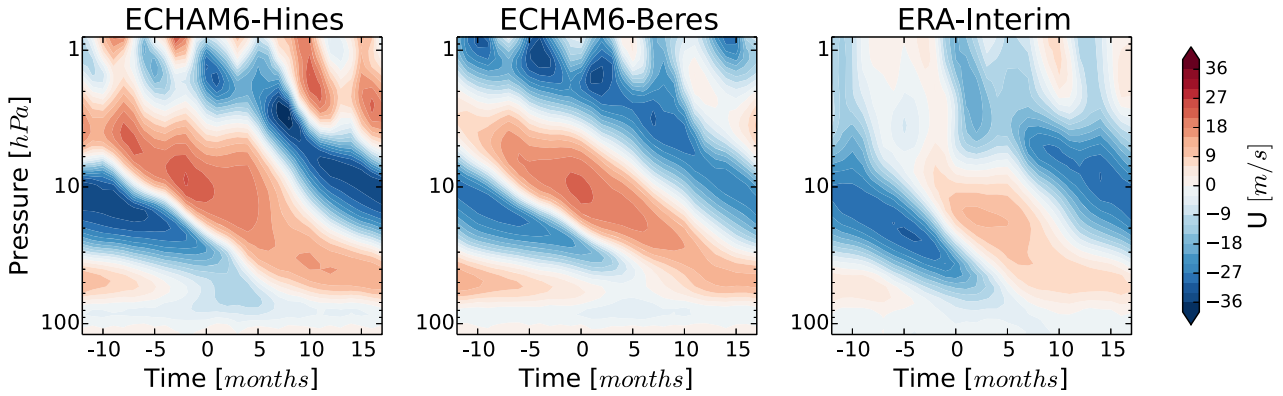

Figure 7. QBO composites of meridional (5°N to 5°S lat) and zonal mean zonal wind. Criterion for the composite is the onset of the westerly jet at 20 hPa. Comparison of the GW parameterization with constant sources (ECHAM6-Hines) with the convection-based GW parameterization (ECHAM6-Beres) and reanalysis (ERA-Interim).

one month and initiated with the same background state. The short temporal coverage guarantees that both parameterizations react to a nearly identical background wind profile. Following *Scaife et al*. [2000], lowering the waves' breaking levels reduces primarily the QBO amplitude. The comparison between both parameterizations shows that the peaks in the drag profile in ECHAM6-Beres are situated at lower altitude than in ECHAM-Hines, thus leading to a reduced QBO amplitude and QBO wind variance.

4.2. Seasonal Effects of Parameterized, Variable GW Sources on the QBO

Due to the physically based GW sources, Figure 1c shows a strong seasonal cycle in the amount of wave momentum flux emanating from the troposphere. We establish a link between the seasonality of GW source strength, the seasonality in the amount of drag in the lower stratosphere, and finally the seasonality of QBO phase progression rate. Following the analysis by *Wallace et al*. [1993], who apply an EOF analysis on the zonal winds, we further extend the concept in order to show the seasonality of individual drag components and of the total drag.

4.2.1. Construction of an EOF Analysis

We apply an EOF analysis on a monthly (t) based time series of meridionally averaged (5°N to 5°S lat) zonal mean anomalies of a variable $\chi'(z,t)$, computed on each vertical level z between 10 and 70 hPa. The analyzed quantities χ' are zonal wind U, total drag on the zonal wind $\frac{\partial U}{\partial t}|_{GWD+\nabla\cdot EP+ADV}$, and the individual drag components due to gravity waves $\frac{\partial U}{\partial t}|_{GWD}$, due to the divergence of the Eliassen-Palm flux of resolved waves, $\frac{\partial U}{\partial t}|_{\nabla\cdot EP}$, and due to horizontal and vertical advection $\frac{\partial U}{\partial t}|_{ADV}$. All data are smoothed by a simple 3 months running average, but in contrast to *Wallace et al*. [1993] and *Taguchi* [2010] not deseasonalized. Each quantity χ' can be expressed as a linear combination of empirical orthogonal functions *EOF*, which are

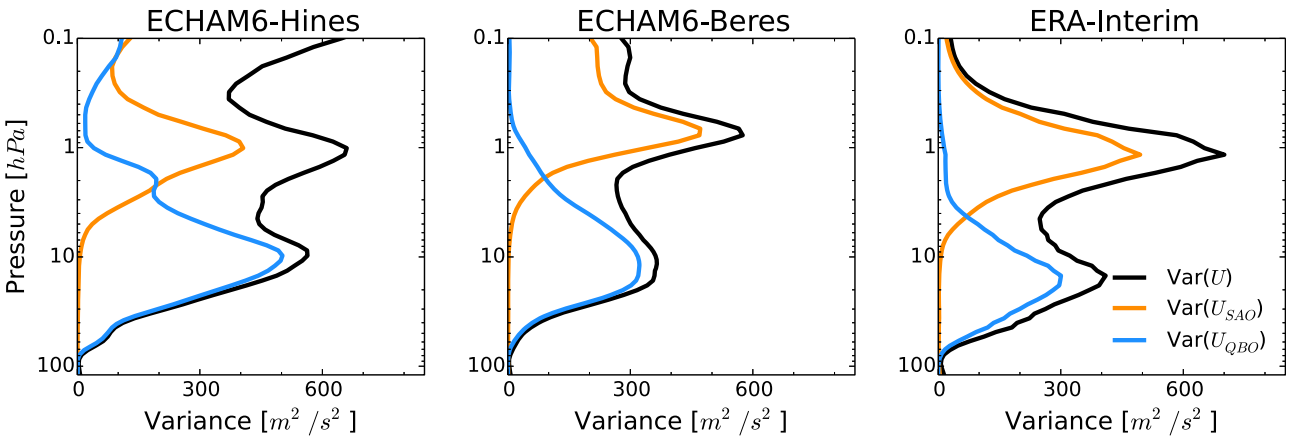

Figure 8. Variance over time (30 years) of meridional (5°N to 5°S lat) and zonal mean zonal wind. In order to compute Var(U_{SAO}) in orange and Var(U_{QBO}) in blue, a Fourier transform in time is applied to the winds, the periods between 5 and 7 months (SAO) and between 23 and 35 months (QBO) are selected to calculate each variance contribution. The variance over all periods Var(U) is depicted in black. Comparison of the GW parameterization with constant sources (ECHAM6-Hines) with the convection-based GW parameterization (ECHAM6-Beres) and reanalysis (ERA-Interim).

dependent on height but constant in time, and principal components *pc* which represent the corresponding time series:

$$\chi'(z,t) \simeq EOF_1(z) \cdot pc_1(t) + EOF_2(z) \cdot pc_2(t) \tag{3}$$

omitting higher orders since the first two *EOF*s cover most of the variance; in the case of *U*, the two leading *EOF*s account for 96.1% of the total variance, see Figure 10a. The *EOF*s of the drag components due to GW and the total drag are shown in Figures 10b and 10c.

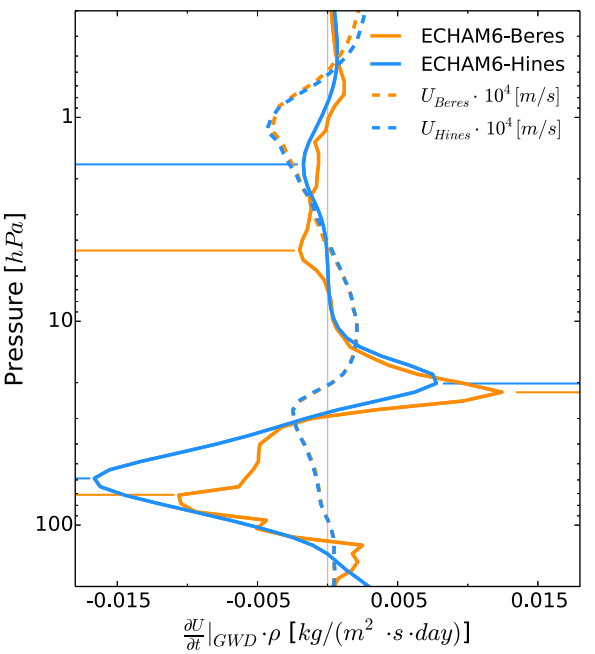

Figure 9. Comparison of GW drag $\left(\frac{\partial U}{\partial t}|_{GWD}\right)$ profiles of ECHAM6-Beres (orange) with ECHAM6-Hines (blue), drag is scaled by density. Maxima in the drag profiles are emphasized by horizontal lines in colors accordingly, wind profiles are dashed. Zonal and meridional (5°N to 5°S lat) mean over one month.

Due to the high amount of covered variance by the two leading *EOF*s, the two-dimensional phase space of the *pcs* serves as a good proxy for the temporal evolution of the QBO, displayed in Figures 10d–10f. Each point $\psi(t)$ in phase space corresponds to a state of the QBO in a certain month, while in the course of a full QBO cycle, the points form a circle in phase space. Given the circular characteristics of the temporal evolution in phase space, the data points ψ can be represented by polar coordinates with the radial coordinate $|\psi|$

$$|\psi(t)| = \sqrt{pc_1(t)^2 + pc_2(t)^2} \tag{4}$$

and angular coordinate ϕ

$$\phi(t) = atan2(pc_1(t), pc_2(t)) \tag{5}$$

with the function *atan*2 being based on the function *arctan*, but extended to return the appropriate quadrant of the computed angle. The function *atan*2 returns a value in [0, 2 π [which correspond to angles of the entire circle.

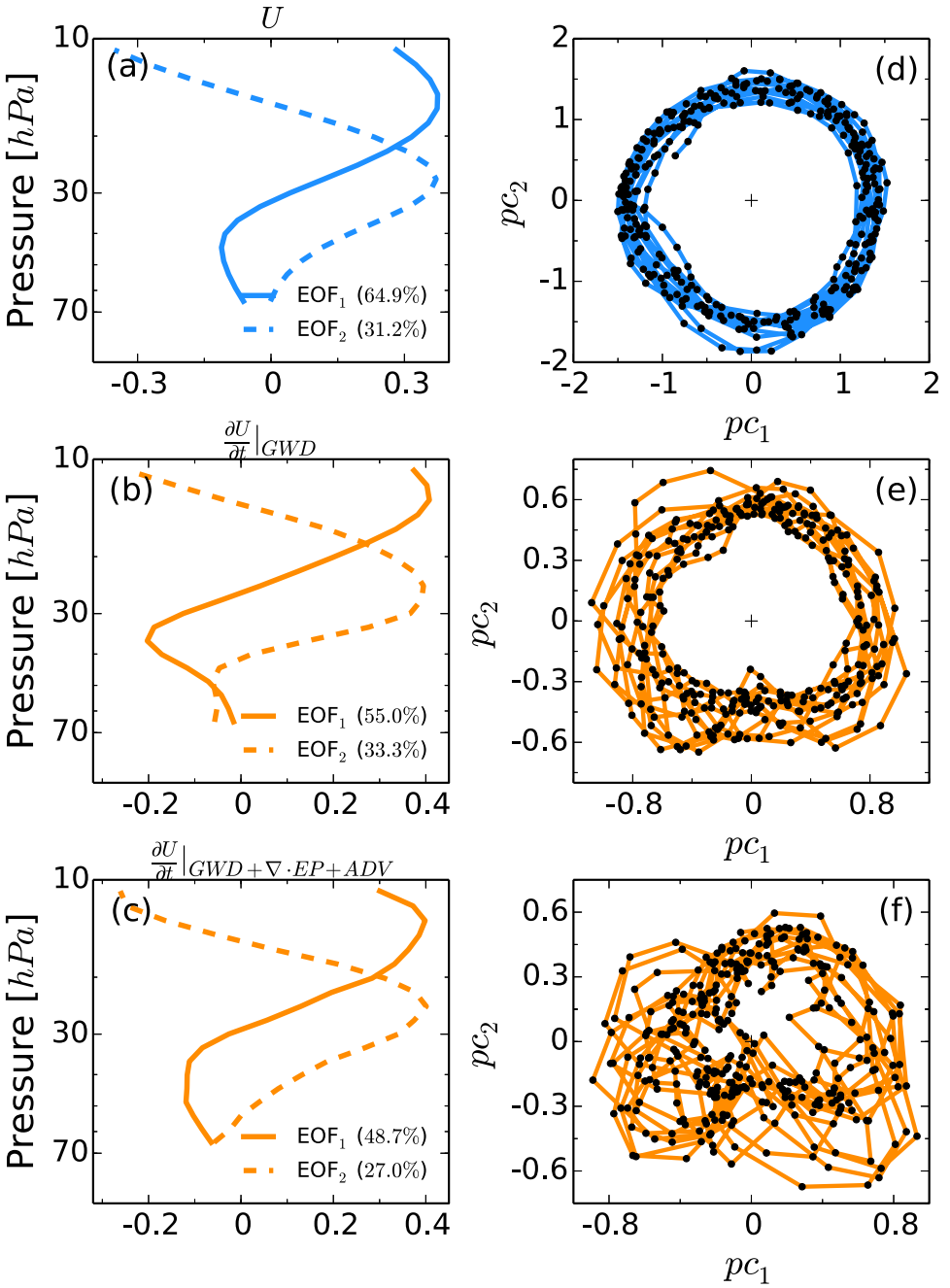

Figure 10. (a–c) Empirical orthogonal functions (*EOF*) and (d–f) principal components (*pc*) of zonal wind *U* (Figures 10a and 10d), GW drag $\frac{\partial U}{\partial t}|_{GWD}$ (Figures 10b and 10e), and the sum of all drag components $\frac{\partial U}{\partial t}|_{GWD+\nabla\cdot EP+ADV}$ (Figures 10c and 10f). The numbers in Figures 10a–10c indicate the fraction of variance that each EOF accounts for. The *pcs* in Figure 10d are scaled to unit variance, units on individual plots are arbitrary. The *EOFs* and *pcs* of $\frac{\partial U}{\partial t}|_{\nabla\cdot EP}$ and $\frac{\partial U}{\partial t}|_{ADV}$ are not shown individually; they are qualitatively similar to $\frac{\partial U}{\partial t}|_{GWC}$ in Figures10b and 10e.

In the case of *U*, we estimate the progression rate of the QBO phase $\phi_U^{'}$ in month *t* as the rate of change of the angle ϕ,

$$\phi_U'(t) = \frac{1}{2\cdot 2\pi}[\phi(t-1)+\phi(t+1)] \tag{6}$$

with the units cycle/month. In the cases when the EOF analysis was applied to the different drag components, we use $|\psi(t)|$ as a proxy for the amount of drag in the particular month. For each month, we calculate

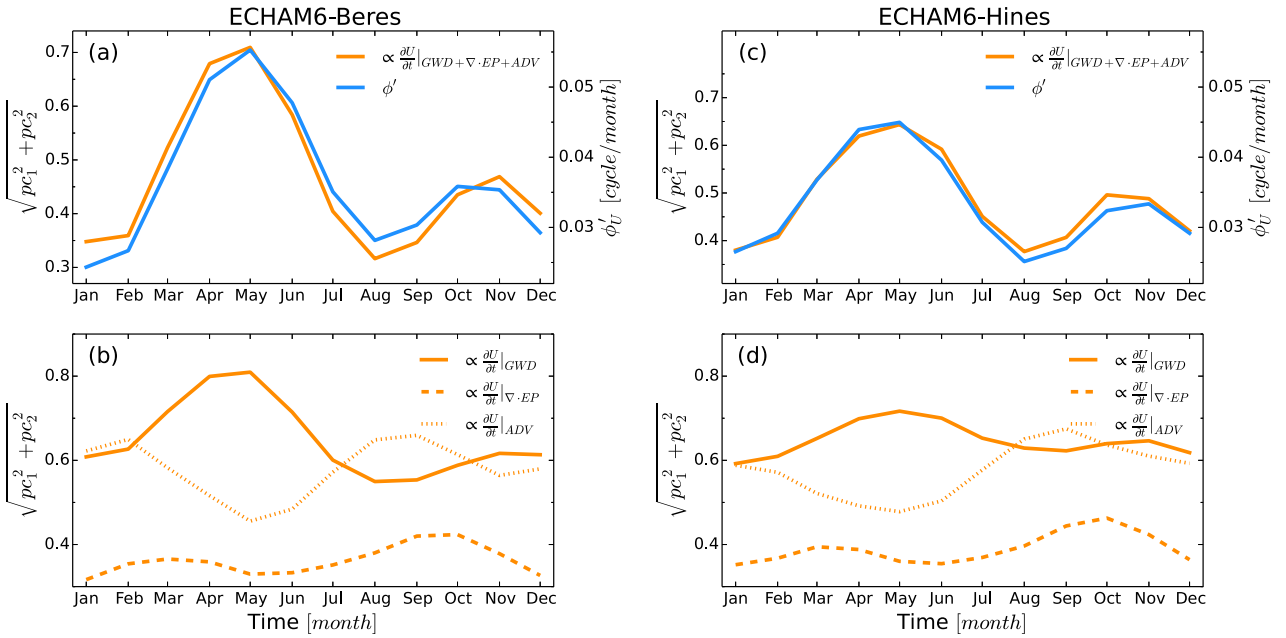

Figure 11. Seasonal cycle of progression of QBO phases (blue) and seasonal cycle of amount of drag (orange) for (a and b) the Beres and (c and d) the Hines scheme. Comparison of QBO phase progression (blue) with amount of all drag components (orange) for the Beres (Figure 11a) and the Hines (Figure 11c) scheme. Comparison of the individual drag components of the entire drag budget for the Beres (Figure 11b) and the Hines (Figure 11d) scheme. The drawn drag is proportional to the actual drag values, units are arbitrary. Note the two different *y* axis in Figures 11a and 11c.

ϕ' from the phase space in *U* and $|\psi|$ for the individual drag components and compile the data to show the seasonality of the computed quantities, displayed in Figure 11.

4.2.2. Results on the Seasonal Time Scale

The seasonality of QBO phase progression and the seasonality of the total drag are in good agreement, peaking in May and showing a second local maximum in October/November, shown for both ECHAM6-Beres in Figure 11a and ECHAM6-Hines in Figure 11c. This objective statistical analysis confirms the physical understanding that the QBO descends faster in times when more drag is exerted. Focusing on the individual drag components in Figures 11b and 11d, we see that each component exhibits different characteristics in seasonality. While $\frac{\partial U}{\partial t}|_{\nabla\cdot EP}$ shows a semiannual oscillatory behavior with peaks in March and October, $\frac{\partial U}{\partial t}|_{ADV}$ has a minimum in late spring and maximum in late summer which opposes the maxima and minima of the entire drag of Figures 11a and 11c. Both $\frac{\partial U}{\partial t}|_{ADV}$ and $\frac{\partial U}{\partial t}|_{\nabla\cdot EP}$ show a qualitatively similar behavior in both model versions. The seasonality of the drag due to GW, however, differs for the different GW parameterizations. While both $\frac{\partial U}{\partial t}|_{GWD}$ in ECHAM6-Hines and $\frac{\partial U}{\partial t}|_{GWD}$ in ECHAM6-Beres show an annual variation with maximum in April/May and minimum in August/September, the seasonality in ECHAM6-Beres is more pronounced which is manifested in the stronger amplitude of the seasonal variation of $\frac{\partial U}{\partial t}|_{GWD}$.

Note that the entire drag in the top part of Figure 11 is not attained by simply adding the three drag components in the bottom part. Each curve is the result of an individual EOF analysis and in the case of the total drag, the individual drag components are added before the EOF analysis is performed.

In Figure 12, the comparison of the two model configurations with observations suggests an improvement due to the variable GW scheme in ECHAM6-Beres. Both model versions show qualitatively a consistent agreement with observations, which is caused by the similar seasonality of $\frac{\partial U}{\partial t}|_{ADV}$. However, adding the seasonal cycle of $\frac{\partial U}{\partial t}|_{GWD}$ in the case of ECHAM6-Beres leads to better agreement with the observed seasonality. Note that the mean phase progression in both ECHAM6-Hines and ECHAM6-Beres lie within the 2σ ranges of the reanalysis product and that the shown improvement in QBO phase progression rate in ECHAM6-Beres is statistically not significant.

5. Discussion and Implications for Tuning the GW Schemes

Most parameterizations include parameters, whose values are only loosely determined by theoretical arguments or observational studies but which substantially impact the output of the parameterization.

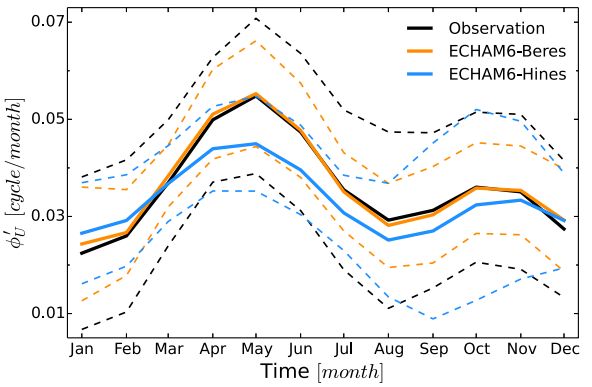

Figure 12. Seasonal cycle of progression of QBO phases ϕ'. The comparison with radiosonde observations from FU Berlin (black) shows an improvement of the convection-based GW parameterization in ECHAM6-Beres (orange) over ECHAM6-Hines with a GW parameterization with constant sources (blue). Dashed lines show the 2σ range.

Changing the value of these parameters within the theoretical and observational limits, in order to generate a more realistic representation of the parameterized processes or affected phenomena, remains a necessary step while implementing a parameterization into a model. Here we refer to this process as "tuning" and to the adjustable parameters as "tuning parameters". In this study, we tune the GW source and GW propagation parameterization in order to obtain a QBO; we specifically choose the QBO period as the most important target criterion. In this section, we focus on two aspects of the source spectrum, the spectral shape and the amplitude, and we evaluate potentials for tuning each of the two aspects in the context of the Beres + AD99 setup.

5.1. Spectral Characteristics of the Source Momentum Fluxes: Tuning the Propagation Scheme

The comparison of convection properties of ECHAM6-Beres with observational products reveals discrepancies which affect the source spectrum's shape. The overrepresentation of deep convective clouds in ECHAM6, Figure 5b, results in large source momentum fluxes at large heating depths, see the peak at 15 km in Figure 5a. This bias at deep convective events leads to an overrepresentation of source momentum fluxes at high phase speeds (Figure 4). Additionally, the design of the Beres scheme already entails an underrepresentation of source momentum flux at low phase speeds. The parameterization does not include the waves generated by the obstacle effect, or "moving mountain mechanism" [*Lane et al*., 2001]. These waves are similar to orographic GW such that the waves are stationary with respect to the convective cell, thus producing momentum fluxes at low phase speeds. For a more detailed discussion on the difficulties of implementing the obstacle effect into GW source parameterizations, see *Alexander et al*. [2006]. The combined effect of both aspects, the bias in the convection scheme and the missing obstacle effect, suggests an underrepresentation of small phase speed waves, $|c_p| < 15\,\mathrm{m/s}$, and an overrepresentation of large phase speed waves, $|c_p| > 40\,\mathrm{m/s}$, in the modeled source spectrum.

Results from other model studies and observations support the existence of a modeled overrepresentation of large phase speed waves and underrepresentation of small phase speed waves. Several case studies performed with cloud resolving models show source spectra which peak in the range between 5 and 20 m/s [*Alexander and Holton*, 1997; *Piani and Durran*, 2001; *Alexander et al*., 2006; *Kuester et al*., 2008]. The observational study based on localized airborne measurements by *Pfister et al*. [1993] reveals source spectra peaking between 0 and 10 m/s, depending on the background wind. *Jewtoukoff et al*. [2013] analyze high frequency balloon measurements in the stratosphere which show GW spectra peaking between 0 and 15 m/s, while corresponding numerical simulations show peaks at higher phase speeds. Even though one referenced spectrum peaks at 20 m/s, which is in accordance with the peak of the modeled source spectrum (Figure 1), none of the referenced spectra shows such pronounced momentum fluxes at phase speeds bigger than 40 m/s.

The Beres scheme provides very limited possibilities for tuning the spectral shape because the spectral characteristics are dependent on the convective properties and the background wind, a fundamental concept of the parameterization. If these physical input values, however, exhibit a robust bias, only a rather brute-force manipulation of the spectral shape is possible, e.g., restricting momentum fluxes to phase speeds < 50 m/s. Even though other studies and observations suggest that the modeled source spectrum shows deficiencies, we refrain from manually changing the source spectrum for two reasons: first, the high degree of unphysical subjectiveness that would be incorporated into the parameterization and second, the lack of sufficient comprehensive observations of global source spectra characteristics.

However, the indicated underrepresentation of momentum fluxes at low phase speeds is reflected in the values chosen for parameters ϵ and λ_h, relevant for tuning the propagation parameterization. A small value of ϵ and a large value for λ_h both decrease the levels where the waves become convectively unstable, the breaking level. When tuning the propagation parameterization, the values for ϵ and λ_h are chosen such that the peaks in the drag profile correspond to the levels of the strongest wind shear. Given the underrepresentation of waves with low phase speeds, a high value for λ_h and a small value for ϵ are necessary so that waves with large phase speeds break at much lower levels than their critical levels.

5.2. Amplitude of the Source Spectrum: Tuning for the QBO Period

The range of total momentum flux excited in the tropics is well observed. Studies based on observations and cloud resolving models show mean momentum fluxes in the range 1–5 mPa [*Sato and Dunkerton*, 1997; *Piani et al*., 2000; *Grimsdell et al*., 2010; *Geller et al*., 2013], while *Dunkerton* [1997] states that it requires time averaged, zonal mean flux of tropical gravity waves of approximately 1 mPa to drive the QBO. The observational data constrain the range of total excited momentum flux for justifiable limits on tuning parameters. The two parameters C_F and L, the fraction of convection within a GCM grid box and the spatial averaging length, respectively, influence the overall amplitude of the source spectrum. The amplitude of the source spectrum affects the amount of exerted drag on the jets of the QBO and consequently strongly determines the QBO period, see also *Scaife et al*. [2000]. Both tuning parameters equally change the amount of momentum flux at all phase speeds of the spectrum but have no effect on the spectral shape or the temporal and spatial variability. The GW source parameterization produces, on an annual average, a mean momentum flux of approximately 3–3.5 mPa, see Figure 1c. Given that the modeled amount of excited wave momentum flux compares well to observations and that with $C_F = 3.5\%$ and $L = 1000$ km the parameter values lie within a physical range, we can say that the tuning of the source parameterization obeys the limits of the observations. The tuned amplitude of the source spectrum generates a QBO period of $\sim$27.5 months.

6. Summary and Conclusions

We couple the convection-based source parameterization of gravity waves (GW) after *Beres et al*. [2004] to the propagation parameterization after *Alexander and Dunkerton* [1999] and implement the schemes into the atmospheric general circulation model ECHAM6. Compared to a GW source parameterization with constant, prescribed sources, the Beres parameterization improves the representation of GWs in two main aspects. First, the excited gravity waves show a strong spatial, Figure 1a, and temporal, Figures 1b and 1c, variability in the amount of total momentum flux. This variability is directly linked to the occurrence of areas of intense convection. Second, the spectral shape characteristics of the source spectrum is not prescribed but coupled to heating characteristics of the convection scheme and the background wind. In detail, regionally different background winds over South America and the Indonesian archipelago result in different shapes of the source spectra, with dominating easterly and westerly waves, respectively (Figure 2). The analysis further reveals that the regime of deep convective clouds causes in large part the spectral asymmetry, because vertical wind shears more effectively affect deep clouds than shallow clouds. Studies [*Pfister et al*., 1993] on localized geographical regions have shown that wind shear causes asymmetries in the waves' source spectrum. Moreover, our model results also show that this effect remains important even when averaging over large geographical domains covering $>$ 10,000 km (order of 100° longitude at the equator). The existence of asymmetric source spectra over large geographical regions has implications for GW source parameterizations with a prescribed source spectrum. Analogous to *Geller et al*. [2011], who prescribe a temporally varying source spectrum in amplitude, the next step would be to include spatially varying asymmetric source spectra.

To the authors knowledge, this is the first time that an atmospheric GCM produces a realistic QBO with a convection-based GW source parameterization as the only source of GWs, see Figure 6. Compared to the previously employed GW parameterization in ECHAM6, which prescribes spatially and temporally constant sources, the QBO simulated with ECHAM6-Beres shows, on one hand, a slight deterioration of the vertical extent of the easterly jet, shown in Figure 7. On the other hand, however, the wind speeds of the jet maxima and the variance of wind alteration show a clear improvement, see Figure 8. More generally, we would like to point out that deficiencies in QBO characteristics are not necessarily linked to shortcomings in GW

parameterizations. Possible deficiencies in the modeled resolved waves or the upwelling will deteriorate the representation of the QBO.

Furthermore, we apply an EOF analysis on the QBO zonal winds and on the individual drag components of the momentum budget of the QBO. The analysis shows that the seasonality of the GW drag dominates the seasonality of the downward propagation of the QBO jets. Note that $\frac{\partial U}{\partial t}|_{GWD}$ in Figure 11b matches the seasonal variation in excited amount of momentum flux in Figure 11c. Due to a more realistic, seasonally varying excitation of parameterized wave fluxes from convection, the modeled QBO suggests an improvement in its jet downward propagation rate, see Figure 12. We point out that the EOF analysis suffers several simplifications: first, the EOF analysis produces only vertically integrated values of QBO related quantities, second the series of *EOF*s is truncated after the first two *EOF*s, and third using the length of the vector in phase space as a proxy for the amount of drag is a crude approximation. However, in contrast to the given shortcomings of the analysis, the strong agreement between the amount of drag and the QBO phase progression in both model versions confirms the applicability of the chosen method, Figures 11a and 11c.

When tuning the parameterization, it turns out that the amplitude of the source spectrum, which translates to the total amount of excited momentum flux, and the breaking levels of the propagation parameterization are important factors to produce a QBO in the chosen model setup. Within the range of physically justified limits, both the amplitude and the breaking levels require tuning. However, the shape, the asymmetries, the temporal, and the spatial variability of the spectrum remain entirely based on physical values, provided by the model. We showed that the physically based character of the source parameterization, coupled to the propagation parameterization of AD99, improves the modeled QBO.

Acknowledgments
We thank the Max Planck Society, the International Max Planck Research School for Earth System Modeling, and the Northwest Research Associates (NWRA-CORA). Support for Joan M. Alexander was provided by grants from the US National Science Foundations Physical and Dynamic Meteorology and Climate and Large-scale Dynamics Programs, ATM-943506 and AGS-1318932. Simulations were carried out on the supercomputing facilities of the German Climate Computation Centre (DKRZ) in Hamburg. Marco Giorgetta and Thomas Krismer provided valuable feedback on earlier drafts of this work. The original code for the Beres parameterization was provided and adopted from WACCM.

References

Alexander, M. J., and T. J. Dunkerton (1999), A spectral parameterization of mean-flow forcing due to breaking gravity waves, *J. Atmos. Sci.*, *56*(24), 4167–4182, doi:10.1175/1520-0469(1999)056¡4167:ASPOMF¿2.0.CO;2.

Alexander, M. J., and J. Holton (1997), A model study of zonal forcing in the equatorial stratosphere by convectively induced gravity waves, *J. Atmos. Sci.*, *54*, 408–419.

Alexander, M. J., J. H. Richter, and B. R. Sutherland (2006), Generation and trapping of gravity waves from convection with comparison to parameterization, *J. Atmos. Sci.*, *63*(11), 2963–2977, doi:10.1175/JAS3792.1.

Alexander, M. J., et al. (2010), Recent developments in gravity-wave effects in climate models and the global distribution of gravity-wave momentum flux from observations and models, *Q. J. R. Meteorol. Soc.*, *136*(650), 1103–1124, doi:10.1002/qj.637.

Baldwin, M. P., et al. (2001), The quasi-biennial oscillation, *Rev. Geophys.*, *39*(2), 179–229.

Beres, J., M. J. Alexander, and J. R. Holton (2002), Effects of tropospheric wind shear on the spectrum of convectively generated gravity waves, *J. Atmos. Sci.*, *59*, 1805–1824.

Beres, J. H., M. J. Alexander, and J. R. Holton (2004), A method of specifying the gravity wave spectrum above convection based on latent heating properties and background wind, *J. Atmos. Sci.*, *61*(3), 324–337, doi:10.1175/1520-0469(2004)061¡0324:AMOSTG¿2.0.CO;2.

Beres, J. H., R. R. Garcia, B. A. Boville, and F. Sassi (2005), Implementation of a gravity wave source spectrum parameterization dependent on the properties of convection in the Whole Atmosphere Community Climate Model (WACCM), *J. Geophys. Res.*, *110*, D10108, doi:10.1029/2004JD005504.

Chun, H.-Y., and J.-J. Baik (2002), An updated parameterization of convectively forced gravity wave drag for use in large-scale models, *J. Atmos. Sci.*, *59*(5), 1006–1017, doi:10.1175/1520-0469(2002)059¡1006:AUPOCF¿2.0.CO;2.

Dee, D. P., et al. (2011), The ERA-Interim reanalysis: Configuration and performance of the data assimilation system, *Q. J. R. Meteorol. Soc.*, *137*(656), 553–597, doi:10.1002/qj.828.

Dunkerton, T. J. (1997), The role of gravity waves in the quasi-biennial oscillation, *J. Geophys. Res.*, *102*(D22), 26,053–26,076.

Fritts, D. C., and M. Alexander (2003), Gravity wave dynamics and effects in the middle atmosphere, *Rev. Geophys*, *41*(1), 1003, doi:10.1029/2001RG000106.

Geller, M. A., T. Zhou, R. Ruedy, I. Aleinov, L. Nazarenko, N. L. Tausnev, S. Sun, M. Kelley, and Y. Cheng (2011), New gravity wave treatments for GISS climate models, *J. Clim.*, *24*(15), 3989–4002, doi:10.1175/2011JCLI4013.1.

Geller, M. A., et al. (2013), A comparison between gravity wave momentum fluxes in observations and climate models, *J. Clim.*, *26*(17), 6383–6405, doi:10.1175/JCLI-D-12–00545.1.

Giorgetta, M. A., E. Manzini, and E. Roeckner (2002), Forcing of the quasi-biennial oscillation from a broad spectrum of atmospheric waves, *Geophys. Res. Lett.*, *29*(8), 1245, doi:10.1029/2002GL014756.

Giorgetta, M. A., et al. (2013), Climate and carbon cycle changes from 1850 to 2100 in MPI-ESM simulations for the coupled model intercomparison project phase 5, *J. Adv. Model. Earth Syst.*, *5*, 572–597, doi:10.1002/jame.20038.

Grimsdell, A. W., M. J. Alexander, P. T. May, and L. Hoffmann (2010), Model study of waves generated by convection with direct validation via satellite, *J. Atmos. Sci.*, *67*(5), 1617–1631, doi:10.1175/2009JAS3197.1.

Hines, C. (1997a), Doppler-spread parameterization of gravity-wave momentum deposition in the middle atmosphere. Part 1: Basic formulation, *J. Atmos. Sol. Terr. Phys.*, *59*(4), 371–386.

Hines, C. (1997b), Doppler-spread parameterization of gravity-wave momentum deposition in the middle atmosphere. Part 2: Broad and quasi monochromatic spectra, and implementation, *J. Atmos. Sol. Terr. Phys.*, *59*(4), 387–400.

Jewtoukoff, V., R. Plougonven, and A. Hertzog (2013), Gravity waves generated by deep tropical convection: Estimates from balloon observations and mesoscale simulations, *J. Geophys. Res. Atmos.*, *118*, 9690–9707, doi:10.1002/jgrd.50781.

Kim, Y.-H., A. C. Bushell, D. R. Jackson, and H.-Y. Chun (2013), Impacts of introducing a convective gravity-wave parameterization upon the QBO in the Met Office Unified Model, *Geophys. Res. Lett.*, *40*, 1873–1877, doi:10.1002/grl.50353.

Kistler, R., et al. (2001), The NCEP-NCAR 50-year reanalysis: Monthly means CD-ROM and documentation, *Bull. Am. Meteorol. Soc.*, *82*(2), 247–267.
Kuester, M. A., M. J. Alexander, and E. A. Ray (2008), A model study of gravity waves over Hurricane Humberto (2001), *J. Atmos. Sci.*, *65*(10), 3231–3246, doi:10.1175/2008JAS2372.1.
Lane, T., M. Reeder, and T. Clark (2001), Numerical modeling of gravity wave generation by deep tropical convection, *J. Atmos. Sci.*, *58*, 1249–1274.
Lott, F., and L. Guez (2013), A stochastic parameterization of the gravity waves due to convection and its impact on the equatorial stratosphere, *J. Geophys. Res. Atmos.*, *118*, 8897–8909, doi:10.1002/jgrd.50705.
Lott, F., and M. Miller (1997), A new subgrid-scale orographic drag parametrization: Its formulation and testing, *Q. J. R. Meteorol. Soc.*, *123*, 101–127.
McFarlane, N. (1987), The effect of orographically excited gravity wave drag on the general circulation of the lower stratosphere and troposphere, *J. Atmos. Sci.*, *44*(14), 1775–1800.
McLandress, C., and J. Scinocca (2005), The GCM response to current parameterizations of nonorographic gravity wave drag, *J. Atmos. Sci.*, *62*(7), 2394–2413.
McLandress, C., M. J. Alexander, and D. L. Wu (2000), Microwave Limb Sounder observations of gravity waves in the stratosphere: A climatology and interpretation, *J. Geophys. Res.*, *105*(D9), 11,947, doi:10.1029/2000JD900097.
Nordeng, T. E. (1994), Extended versions of the convective parameterization scheme at ECMWF and their impact on the mean and transient activity of the model in the tropics, *Tech. Memo. 206*, Eur. Cent. for Medium Range Weather Forecasts, Reading, U. K.
Ortland, D. A., and M. J. Alexander (2006), Gravity wave influence on the global structure of the diurnal tide in the mesosphere and lower thermosphere, *J. Geophys. Res.*, *111*, A10S10, doi:10.1029/2005JA011467.
Ortland, D. A., M. J. Alexander, and A. W. Grimsdell (2011), On the wave spectrum generated by tropical heating, *J. Atmos. Sci.*, *68*(9), 2042–2060, doi:10.1175/2011JAS3718.1.
Pfister, L., S. Scott, M. Lowenstein, S. Bowen, and M. Legg (1993), Mesoscale disturbances in the tropical stratosphere excite by convection: Observations and effects on the stratospheric momentum budget, *J. Atmos. Sci.*, *50*(8), 1058–1075.
Piani, C., and D. Durran (2001), A numerical study of stratospheric gravity waves triggered by squall lines observed during the TOGA COARE and COPT-81 experiments, *J. Atmos. Sci.*, *58*, 3702–3723.
Piani, C., D. Durran, M. J. Alexander, and J. R. Holton (2000), A numerical study of three-dimensional gravity waves triggered by deep tropical convection and their role in the dynamics of the QBO, *J. Atmos. Sci.*, *57*(22), 3689–3702, doi:10.1175/1520-0469(2000)057¡3689:ANSOTD¿2.0.CO;2.
Richter, J. H., F. Sassi, and R. R. Garcia (2010), Toward a physically based gravity wave source parameterization in a general circulation model, *J. Atmos. Sci.*, *67*(1), 136–156, doi:10.1175/2009JAS3112.1.
Ryu, J.-H., M. J. Alexander, and D. A. Ortland (2011), Equatorial waves in the upper troposphere and lower stratosphere forced by latent heating estimated from TRMM rain rates, *J. Atmos. Sci.*, *68*(10), 2321–2342, doi:10.1175/2011JAS3647.1.
Salby, M., and R. Garcia (1987), Transient response to localized episodic heating in the tropics. Part I: Excitation and short-time near-field behavior, *J. Atmos. Sci.*, *44*(2), 458–498.
Sato, K., and T. Dunkerton (1997), Estimates of momentum flux associated with equatorial Kelvin and gravity waves, *J. Geophys. Res.*, *102*(D22), 26,247–26,261.
Scaife, A., N. Butchart, C. D. Warner, D. Stainforth, W. Norton, and J. Austin (2000), Realistic quasi biennial oscillations in a simulation of the global climate, *Geophys. Res. Lett.*, *27*(21), 3481–3484.
Schmidt, H., et al. (2013), Response of the middle atmosphere to anthropogenic and natural forcings in the CMIP5 simulations with the Max Planck Institute Earth system model, *J. Adv. Model. Earth Syst.*, *5*, 98–116, doi:10.1002/jame.20014.
Shibata, K., and M. Deushi (2005), Partitioning between resolved wave forcing and unresolved gravity wave forcing to the quasi-biennial oscillation as revealed with a coupled chemistry-climate model, *Geophys. Res. Lett.*, *32*, L12820, doi:10.1029/2005GL022885.
Song, I., H. Chun, and T. Lane (2003), Generation mechanisms of convectively forced internal gravity waves and their propagation to the stratosphere, *J. Atmos. Sci.*, *60*, 1960–1980.
Stevens, B., et al. (2013), Atmospheric component of the MPIM Earth System Model: ECHAM6, *J. Adv. Model. Earth Syst.*, *5*, 1–27, doi:10.1002/jame.20015.
Taguchi, M. (2010), Observed connection of the stratospheric quasi-biennial oscillation with El Niño-Southern Oscillation in radiosonde data, *J. Geophys. Res.*, *115*, D18120, doi:10.1029/2010JD014325.
Tiedtke, M. (1989), A comprehensive mass flux scheme for cumulus parameterization in large-scale models, *Mon. Weather Rev.*, *117*(8), 1779–1800.
Wallace, J., R. Panetta, and J. Estberg (1993), Representation of the equatorial stratospheric quasi-biennial oscillation in EOF phase space, *J. Atmos. Sci.*, *50*(12), 1751–1762.